Stability Analysis of Whirl Flutter in a Nonlinear Gimballed Rotor-Nacelle System

Christopher Mair
PhD Researcher
University of Bristol
United Kingdom

Djamel Rezgui
Lecturer
University of Bristol
United Kingdom

Branislav Titurus
Senior Lecturer
University of Bristol
United Kingdom

ABSTRACT

Whirl flutter is an aeroelastic instability that affects propellers/rotors and the aircraft on which they are mounted. The complexity of its behaviour and analysis increases significantly with the addition of nonlinear effects. With their long and flexible rotor blades, tiltrotor aircraft are particularly susceptible. This paper investigates the impact of structural nonlinearity on the whirl flutter stability of a basic gimballed rotor-nacelle model, compared to a baseline linear stiffness version. A 9-DoF model with quasi-steady aerodynamics and blades that can move both cyclically and collectively in both flapping and lead-lag motions was adopted from existing literature. The nonlinearities investigated in this paper are cubic and quintic softening and hardening introduced to the gimbal flapping stiffness. The investigation is conducted through a combination of bifurcation and eigenvalue analyses, supplemented by time simulations. In some cases, the nonlinearities are shown to cause whirl flutter behaviour to exist in parameter value regions that are predicted to be stable by linear analysis. This impact is fully captured in the redrawn system stability boundary.

INTRODUCTION

Tiltrotor aircraft such as the XV-15 shown in Figure 1 are a technology area of growing importance due to their unique flight envelope. In addition to a range of mission capabilities, the tiltrotor's flight envelope also offers a potential solution to the airport congestion problem worldwide. This idea requires tiltrotors with the passenger capacity of a regional jet to be developed, which is substantially larger than any existing models. The aero-elastic instability known as whirl flutter is an important consideration in the design of tiltrotors, particularly in the presence of nonlinearity and uncertainty. However, there is little mention in existing literature of nonlinear whirl flutter studies being conducted. In the design of larger tiltrotor aircraft this shortcoming could be a significant liability (Ref. 1) due to uncertainty in how the driving physical phenomena scale with size.

Whirl flutter affects rotors and propellers mounted in wing nacelles. In its most basic form, the whirl flutter motion involves the hub whirling in a circle around its undeformed position when viewed from in front. The physical mechanisms driving the instability are aerodynamics from the rotor blades and wing, gyroscopic effects from the rotor as a whole, and elastic wing structural modes. All three mechanisms contribute significant coupling to the system. Whirl flutter oscillations can damage or even destroy an aircraft (Ref. 3). With their large and flexible blades, tiltrotors are particularly susceptible to whirl flutter.

Figure 1: XV-15 tiltrotor aircraft (Ref. 2)

In both civil and military applications, it is attractive to the operator to maximise the productivity of any aircraft used. Traditionally defined as being a function of payload capacity and cruising speed, current research is dedicated to increasing both. It is in addressing the latter consideration that the problem of whirl flutter is encountered. A given rotor-nacelle system typically encounters the instability above a certain airspeed, when the aerodynamic forces and moments are of sufficient magnitude. For a given cruising speed requirement, whirl flutter safety margin is one of the main design drivers

Presented at the Vertical Flight Society's 75th Annual Forum & Technology Display, Philadelphia, PA, USA, May 13-16, 2019.

for tiltrotor rotor-nacelle-wing systems, and the phenomenon generally limits their maximum forward speed (Ref. 4). However, whirl flutter is also sensitive to the various inertial, damping and stiffness properties of the rotor-nacelle system, which are controllable to varying degrees during the aircraft's design.

Whirl flutter is just one of several different types of instability that may be experienced by a rotor-nacelle system, such as ground resonance or air resonance. The in-plane and out-of-plane stiffnesses of the rotor have significant effects on the stability properties of a rotor-nacelle system with regard to each type of instability. However, these instabilities are discussed in various other works (Refs. 5 and 6); only whirl flutter is investigated in this paper.

The current literature has investigated methods of improving whirl flutter stability margins through both active (Ref. 7) and passive means, such as alterations to existing rotor designs (Ref. 8). Extensive research has also been conducted into understanding the relative sensitivity of whirl flutter to parameters such as control system stiffness (Ref. 1) or rotor blade sweep (Ref. 9). However, in many cases, these studies restricted the modelling of the structural stiffness to linear approximations, which is contingent on the assumption of small deformations. Where nonlinear structural stiffnesses were used, linear analysis methods were ultimately employed. Park et al. investigated whirl flutter with a nonlinear structural model (Ref. 10), though the focus of the paper was an overall design optimization framework as opposed to any impacts on the whirl flutter predictions made by using nonlinear elements in the model. Similarly, investigations by Janetzke et al. (Ref. 11) used nonlinear aerodynamic models adapted from aerofoil data, though the structural aspects of the model did not appear to have benefitted from the same approach.

However, various kinds of nonlinearity have been shown to have a non-negligible effect on system behaviour. Masarati et al. (Ref. 12) showed that nonlinear effects at the blade level can have a knock-on effect on overall system stability, and Krueger (Ref. 13) showed that nonlinearities introduced by the influence of the drivetrain, free-play and backlash can create a behavioural discrepancy between rotors in windmill and thrust mode. While the main focus of Krueger's paper is to present a multibody modelling approach of an existing ADYN wind tunnel test, the effects of nonlinearity were investigated through the introduction of nonlinear springs in the computational model. Spring stops were also added to provide hard limits on model deflection and a good agreement with the wind tunnel test data was shown. Nonlinear effects are therefore an important modelling consideration, especially in the development of new large tiltrotor aircraft.

Sources of nonlinearity in a tiltrotor rotor-nacelle system may be the drivetrain (Ref. 13), as previously mentioned, though other sources may include the deformability of the rotor blades or joint deadband (Ref. 12). Freeplay may also exist at hinges (Ref. 14). In general, the assumption of linear stiffness is only really representative of physical structures when deformations are small – a condition that may well not hold for whirl flutter oscillations – and polynomial softening and/or hardening terms may describe stiffness profiles at larger deflections more realistically (Ref. 15).

The application of continuation and bifurcation methods has so far been limited to a small number of helicopter dynamical problems (Ref. 16), such as flight mechanics, ground resonance and rotor vortex ring state, though their inclusion in rotary wing studies is steadily becoming more prevalent as they are powerful in solving problems such as the identification of instability scenarios of rotor blades (Ref. 17). Continuation methods were used in the AW159/Wildcat Release to Service document (Ref. 18).

The authors have previously explored the effects of nonlinearities on the whirl flutter stability of basic rotor-nacelle system (Refs. 19 and 20). The system was found to have considerably complex dynamics despite its simplicity. Using continuation methods, it was found that the nonlinearities introduced had a substantial effect on the dynamics of the system as compared to the linear baseline version, sometimes creating the possibility of flutter behaviour when linear analysis predicted stability. While the model was adequate for describing whirl flutter, the lack of a gimballed hub prevented robust comparison to tiltrotor models. This shortcoming is addressed via the model's additional features, along with the use of parameter values that describe a full-size system.

Current tiltrotor aircraft use gimballed proprotor hubs, as the lack of bearings allows a weight saving. Additionally, the flapping motion is replaced with hub tilt, which lowers Coriolis-induced loads (Ref. 21). This in turn allows the consideration of lightweight, stiff in-plane rotor blades that have a first in-plane frequency above one-per-rev, which eliminates the possibility of ground resonance. The use of a gimbal at the hub may have a destabilising effect on the rotor's dynamics, however. Additionally, the gimbal may itself be a source of structural nonlinearity if elastomeric materials are used therein to provide elastic restraint. Reed developed the first numerical model for investigating whirl flutter in a basic rotor-nacelle system in 1966 (Ref. 22), though the first tiltrotor-specific model – with features such as a gimballed hub – was developed by Johnson (Ref. 23) in 1974. Johnson gradually incorporated enhancements to the model such as more advanced blade modelling (Ref. 24), though when sufficient computing power became available, the CAMRAD software package (Ref. 25) was instead adopted by research efforts (Refs. 1, 8 and 9). The software provides aeromechanical analysis of helicopters and rotorcraft and was also developed by Johnson.

The aim of this paper is to build on the authors' previous work by using a more detailed model that is more representative of a tiltrotor. The effects of nonlinearities on the stability envelope, as found by continuation analysis, is discussed. A

gimballed rotor-nacelle whirl flutter model is presented in the Whirl Flutter Model section. Both the original form and a nonlinear adaption are presented. The latter includes nonlinear stiffness terms in gimbal flapping, specifically hardening and softening effects provided by terms proportional to the cube and fifth power of the displacement. A derivation of these additional nonlinear terms introduced to the equations is provided. The stability analysis methods are described in the following section and these are applied to the linear and nonlinear models as appropriate. The analysis was carried out for a number of cases to study the effects of nonlinearity for a set of selected parameters. The stability results and bifurcation diagrams generated are discussed in the Results and Discussion section, including redrawn stability boundaries to account for the effects of nonlinearity on whirl flutter stability that are not captured by linear analysis.

WHIRL FLUTTER MODEL

This research uses the 18-state, 9-DoF model used in (Ref. 23). In this model, an *N*-bladed rotor of radius *R* spins with angular velocity Ω at the end of a shaft of length *h*. The shaft is attached to the tip of a single cantilever wing of span *y*. The motion of the shaft is expressed in terms of the elastic deformation of the wing: beamwise/flapwise bending q_1, chordwise bending q_2 and torsion *p*. Modal representations are used for these degrees of freedom. Aggregated damping and stiffness properties are associated with each of these wing degrees of freedom. Additionally, the rotor is attached to the end of the shaft via a gimballed hub, whereby it may itself pitch and yaw about this point, separately from the motion of the shaft. The flapping and lead-lag motions of the individual blades are summed using Fourier coefficients to enable transformation from the rotating frame into the non-rotating frame from which the whole system is viewed. The flapping of the blades in the non-rotating frame constitutes the aforementioned gimbal pitch and yaw degrees of freedom, β_{1C} and β_{1S} respectively, while the lead-lag is manifested as the rectilinear motion of the rotor's centre of gravity within the hub plane, laterally (ζ_{1C}) and vertically (ζ_{1S}). Collective blade motions are also modelled: as coning β_0 (collective flap) and as rotor speed perturbations ζ_0 (collective lead-lag). The stiffnesses of the blade flapping and lead-lag, both cyclic and collective, is modelled implicitly, being specified in terms of the per-rev natural frequency of each motion. The various system components are assigned their own inertial properties. The system schematic is shown in Figure 2.

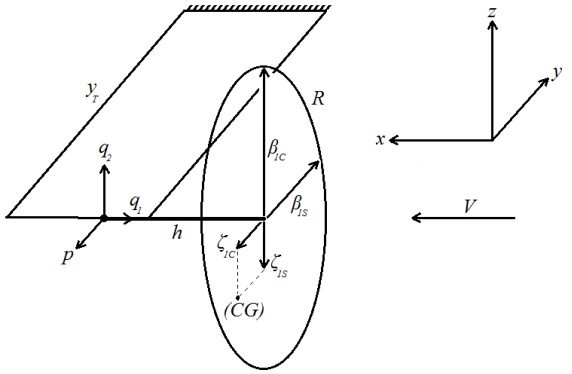

Figure 2: Whirl flutter model schematic adopted from Ref. 23

The aerodynamics of both the blades and the wing are modelled using quasi-steady strip theory (Ref. 26). The derivation uses integrals along each blade, summed, and named according to their origin and the direction of their action. The model also allows for the system to perform in both powered and autorotation regimes of operation. Johnson mentions that proprotor dynamics wind tunnel tests at the time of writing frequently operated the rotor in autorotation and uses it as the first point of reference in his results. The present work uses the data pertaining to the autorotation regime for the purposes of validation, though thereafter the model is operated in the powered condition to maintain relevance to real world operation of tiltrotor aircraft.

Only the first mode of the blade motions (both flap and lead-lag) and the wing motions are considered, due to their negligible participation of higher modes in the coupled wing-rotor motion. Additionally, the motions are not considered to be uncoupled to each other. Also neglected are the aircraft's rigid body motions, since these typically have low frequency and are not highly coupled with the wing and rotor motions. Modelling the system in this way – as a cantilever wing with a fixed end – is generally representative of the wind tunnel testing configuration of proprotor models at this time.

The original model provided features linear structural stiffness properties and was used as a baseline for comparison with the nonlinear stiffness versions. The equations of motion governing the system, as given by (Ref. 23), are too long to write here. However, adopting their original notation, they can be written in the following compact form:

$$\mathbf{M}\ddot{\mathbf{X}} + \mathbf{C}\dot{\mathbf{X}} + \mathbf{K}\mathbf{X} = \mathbf{0} \tag{1}$$

where **M** is the mass matrix, **C** is the damping matrix, **K** is the stiffness matrix and **X** is the degrees of freedom vector. The matrices contain both structural and aerodynamic terms. For the nonlinear modelling, a quintic polynomial expression was used in place of the original linear expressions for the gimbal flapping stiffness. The form of the equation for an arbitrary deflection variable ϵ is given in Equation (2). The 'nl' subscript denotes 'nonlinear'. The influence of each term

is controlled via dedicated coefficients. Rather than being a fixed quantity, the stiffness parameter is now a function of the deflection variable.

$$K_{nl}(\epsilon)\epsilon = K_1\epsilon + K_2\epsilon^3 + K_3\epsilon^5 = (K_1 + K_2\epsilon^2 + K_3\epsilon^4)\epsilon \quad (2)$$

The nonlinear stiffness expression can provide hardening behaviour by using positive values of K_2 or K_3, and softening behaviour by using negative values. The cubic term is dominant at smaller deflections, while the quintic term is dominant at larger deflections, allowing both softening and hardening behaviour to be observed in the same stiffness profile if K_2 and K_3 have opposite signs. Hereafter, a system employing the original linear stiffness expression is referred to as the "linear system", and the systems employing the nonlinear stiffness expression the "softening system", "hardening system" or "combined system" as appropriate. To demonstrate the general shapes of the nonlinear stiffness profiles, the relationship between an arbitrary deflection variable ε and an associated restoring force or moment *M*, compared to the original linear model (i.e. K_2=K_3=0), is demonstrated in Figure 3.

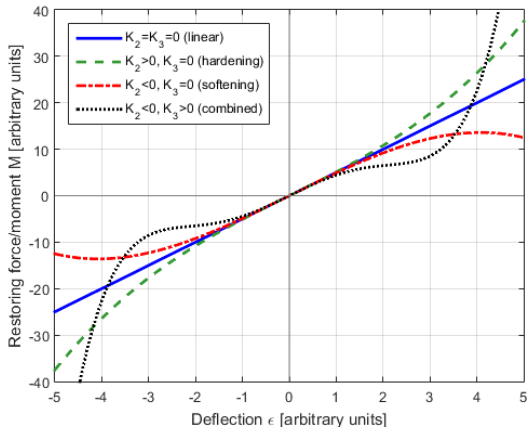

Figure 3: Example nonlinear load-deflection profiles

The derivation of the original model in Ref. 23 presents an equation for the flapping angle β_m of the m^{th} of *N* blades:

$$\beta_m'' + \nu_\beta^2\beta_m - (\alpha_y'' - 2\alpha_x')\cos\psi_m + (\alpha_x'' + 2\alpha_y')\cos\psi_m = \gamma\frac{\tilde{M}_{F_m}}{a\bar{c}} \quad (3)$$

where ν_β is the normalised blade flapping natural frequency, $\alpha_{x,y}$ are shaft yaw and pitch respectively, ψ_m is the azimuth position of the m^{th} blade, $\tilde{M}_{F_M}$ is the normalised aerodynamic moment acting on the m^{th} blade, a is the blade 2D lift slope, $\bar{c}$ is the normalised rotor chord, and dash superscripts denote time differentials in the azimuth domain (i.e. per-rev rather than per second). The flapping motion of the m^{th} blade can be represented by:

$$\beta_m = \beta_0 + \sum_{n=1}^{\Delta}(\beta_{nc}\cos n\psi_m + \beta_{ns}\sin n\psi_m) + \beta_{N/2}(-1)^m \quad (4)$$

As *N* is odd in the parameter value set used, the reactionless flapping mode $\beta_{N/2}$ does not form part of the definition and Δ is defined as $\frac{N-1}{2}$, indicating that for *N*=3 only the first harmonics are required:

$$\beta_m = \beta_0 + \beta_{1c}\cos\psi_m + \beta_{1s}\sin\psi_m \quad (5)$$

Fourier coefficients are used to transform the equations into the non-rotating frame by introducing the following new degrees of freedom:

$$\beta_0 = \frac{1}{N}\sum_{m=1}^{N}\beta_m \quad (6)$$

$$\beta_{1c} = \frac{2}{N}\sum_{m=1}^{N}\beta_m\cos\psi_m \quad (7)$$

$$\beta_{1s} = \frac{2}{N}\sum_{m=1}^{N}\beta_m\sin\psi_m \quad (8)$$

Nonlinear stiffness terms of the form previously described can be added to the flapping equation of the m^{th} blade:

$$\beta_m'' + \nu_\beta^2\beta_m - (\alpha_y'' - 2\alpha_x')\cos\psi_m + (\alpha_x'' + 2\alpha_y')\cos\psi_m + K_2\beta_m^3 + K_3\beta_m^5 = \gamma\frac{\tilde{M}_{F_m}}{a\bar{c}} \quad (9)$$

Note that the normalization by I_b and Ω^2 used in the original derivation is implicit in the nonlinear coefficient nomenclature used here. These nonlinear terms can simply be replaced with the appropriate polynomial expansions of Equation (5). The derivation finishes by summing the set of *N* blade equations with the following operations:

$$\frac{1}{N}\sum_{m=1}^{N}() \quad (10)$$

$$\frac{2}{N}\sum_{m=1}^{N}()\cos\psi_m \quad (11)$$

$$\frac{2}{N}\sum_{m=1}^{N}()\sin\psi_m \quad (12)$$

These allow the various β_m terms in the *N* blade equations to be expressed in terms of the nonrotating degrees of freedom given in Equations (6)-(8), creating three equations that correspond to the β_0, β_{1c} and β_{1s} equations, respectively:

$$\beta_0'' + \nu_\beta^2\beta_0 = \gamma\frac{\tilde{M}_{F_m}}{a\bar{c}} \quad (13)$$

$$\beta_{1C}'' + 2\beta_{1S}' + (\nu_\beta^2 - 1)\beta_{1C} - \alpha_y'' + 2\alpha_x' = \gamma\frac{\tilde{M}_{F_{1C}}}{a\bar{c}} \quad (14)$$

$$\beta_{1S}'' - 2\beta_{1C}' + (\nu_\beta^2 - 1)\beta_{1S} + \alpha_x'' + 2\alpha_y' = \gamma\frac{\tilde{M}_{F_{1S}}}{a\bar{c}} \quad (15)$$

As the polynomial expansions of β_m are in terms of the nonrotating degrees of freedom, the summation of these terms across the *N* blades needs only the substitution of the trigonometric identities for their known corresponding

numerical values (0, ½, etc.). This results in the following additions to the β_0, β_{1c} and β_{1s} equations, respectively:

$$\begin{aligned}\beta_0''+\ldots+(\beta_0(8K_3\beta_0^4+40K_3\beta_0^2\beta_{1c}^2+40K_3\beta_0^2\beta_{1s}^2\\+8K_2\beta_0^2+15K_3\beta_{1c}^4+30K_3\beta_{1c}^2\beta_{1s}^2\\+12K_2\beta_{1c}^2+15K_3\beta_{1s}^4+12K_2\beta_{1s}^2))/8=\ldots\end{aligned} \quad (16)$$

$$\begin{aligned}\beta_{1c}''+\ldots+(\beta_{1c}(40K_3\beta_0^4+60K_3\beta_0^2\beta_{1c}^2+60K_3\beta_0^2\beta_{1s}^2\\+24K_2\beta_0^2+5K_3\beta_{1c}^4+10K_3\beta_{1c}^2\beta_{1s}^2\\+6K_2\beta_{1c}^2+5K_3\beta_{1s}^4+6K_2\beta_{1s}^2))/8=\ldots\end{aligned} \quad (17)$$

$$\begin{aligned}\beta_{1s}''+\ldots+(\beta_{1s}(40K_3\beta_0^4+60K_3\beta_0^2\beta_{1c}^2+60K_3\beta_0^2\beta_{1s}^2\\+24K_2\beta_0^2+5K_3\beta_{1c}^4+10K_3\beta_{1c}^2\beta_{1s}^2\\+6K_2\beta_{1c}^2+5K_3\beta_{1s}^4+6K_2\beta_{1s}^2))/8=\ldots\end{aligned} \quad (18)$$

The gimbal attachment of the rotor disc to the shaft means that cyclic flapping manifests as pitch and yaw of the rotor disc, and collective flapping manifests as coning of the rotor disc. Although the original form of the equations of motion does allow the artificial creation of separate pitch, yaw and collective blade flapping stiffnesses, such a method is too abstract to be of use due to its physical impossibility. A given rotor blade's flapping stiffness is defined relative to the hub with which it rotates, i.e. in the rotating frame. It is therefore not physically realisable in this case to have separate pitch and yaw stiffnesses in the non-rotating frame of reference.

The blade lead-lag equations were left in their original form with linear stiffness. The model equations were written in state-space form, as shown in (19)-(21).

$$\dot{\mathbf{Y}} = f(\mathbf{Y},\mathbf{p}), \mathbf{Y}\in\mathbb{R}^{18}, \mathbf{p}\in\mathbb{R}^{n} \quad (19)$$

$$\mathbf{Y} = \begin{bmatrix}\mathbf{X}\\ \dot{\mathbf{X}}\end{bmatrix} \quad (20)$$

$$\mathbf{X} = [\beta_{1C} \quad \beta_{1S} \quad \zeta_{1C} \quad \zeta_{1S} \quad \beta_0 \quad \zeta_0 \quad q_1 \quad q_2 \quad p]^T \quad (21)$$

Where **Y** is the state vector, **X** is the degree of freedom vector and **p** is a vector of parameters. The models were implemented in MATLAB R2015a using the state vector given in Equation (20). Time simulations were generated using the ode45 solver. The parameter values used throughout the investigation were retained from Ref. 23, and a selection of particularly relevant parameters is listed in Table 1. All dimensionless quantities have been normalised in the same manner as in Ref. 23: rotor quantities with blade inertia I_b and wing quantities with $I_b.N/2$. Johnson gives the parameter values for a wing and two different full-size rotors: a gimballed stiff in-plane rotor and a hingeless soft in-plane rotor. Those describing the former, a 25-ft Bell rotor, have been used here.

Table 1. Datum parameter values used in current model.

Characteristic	English	Metric
Number of blades	3 [-]	
Rotor angular velocity	458 rpm	48 rad/s
Freestream velocity	250 kts	128.61 m/s
Lock number	3.83 [-]	
Advance ratio	0.7 [-]	
Wing beam-wise bending stiffness	18.72 [-]	
Wing chord-wise bending stiffness	50.7 [-]	
Wing torsional stiffness	3.595 [-]	
Wing beam-wise bending damping constant	0.880 [-]	
Wing chord-wise bending damping constant	2.670 [-]	
Wing torsional damping constant	0.093 [-]	
Blade dimensional inertia	105 slugft^2	142 kgm^2
Blade cyclic flapping inertia	1 [-]	
Blade collective flapping inertia	0.779 [-]	
Blade cyclic lead-lag inertia	0.670 [-]	
Blade collective lead-lag inertia	1 [-]	

STABILITY ANALYSIS METHODS

Initially, eigenvalue analysis was used to assess the stability of the linear system. This standard method places the equations of motion of the system in state-space form in order to obtain the Jacobian matrix ***J***, defined as:

$$\dot{\mathbf{Y}} = \mathbf{J}\mathbf{Y} \quad (22)$$

where **Y**, the state vector, is defined as in Equation (20). Given the form of the linear system's equations of motion, as shown in Equation (1), the Jacobian matrix for this system is therefore:

$$\mathbf{J} = \begin{bmatrix}\mathbf{0} & \mathbf{I}\\ -\mathbf{M}^{-1}\mathbf{K} & -\mathbf{M}^{-1}\mathbf{C}\end{bmatrix} \quad (23)$$

where **0** and **I** are 9x9 zero and identity matrices, respectively. The eigenvalues of the Jacobian matrix contain information about the decay rate (i.e. stability) and frequency of the

system's vibrational modes, and the corresponding right eigenvectors contain the mode shapes. Scripts for eigenvalue analysis were written in MATLAB so that a direct interface with the model was possible.

Within Ref. 23 Johnson also presents a wealth of validation material. Shown in Figure 4 is a root locus plot over a sweep of airspeeds of the implemented model's modes as compared to the corresponding figure shown in the original paper. Covering an airspeed range of 25 to 600kts, the roots were found using the method previously described. A good agreement is found between the results of the implemented model and the original model. Johnson's naming of the modes (as shown in the legend of Figure 4) closely follows the naming of the degrees of freedom. Eigenvector component analysis suggests that this may be mainly attributable to prominent participation of certain degrees of freedom in each mode.

The damping ratio of the modes during the same sweep is shown in Figure 5. There is further good agreement between Johnson's data and the outputs from the implemented model. There is correct prediction of the two instabilities shown in the original figure, specifically the q_1 mode at approximately 500 knots and subsequently the q_2 mode at approximately 575 knots. Both are indicated with dashed red lines, and the datum airspeed (128.6 ms^{-1} = 250 kts) is indicated with a dashed black line.

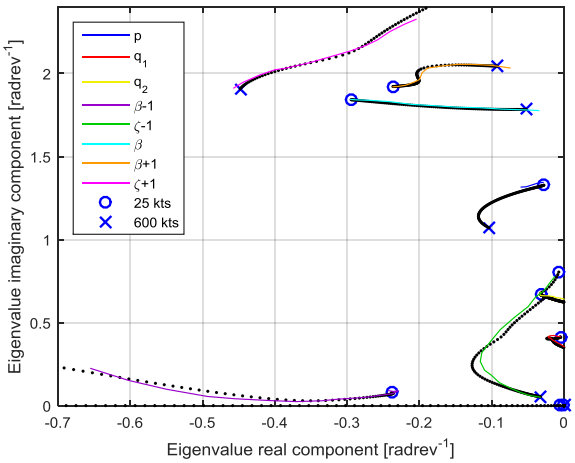

Figure 4: Root loci comparison of current model's results (black dots) with results from Johnson's report (see legend), between 25 to 600kts.

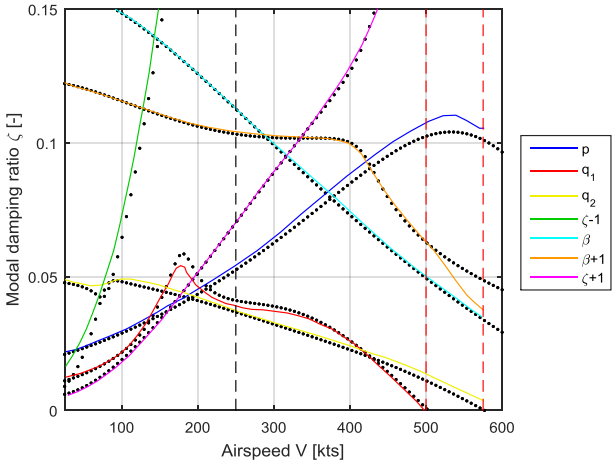

Figure 5: Modal damping ratio comparison of current model's results (black dots) with results from Johnson's report (see legend), between 25 to 600kts.

For nonlinear systems, numerical continuation and bifurcation theory are used. Continuation calculates the steady-state solutions of a dynamical system as one of its parameters, called the continuation parameter, is varied (Ref. 17). The computed solutions construct a number of branches that can be either stable or unstable. To determine their stability, either an eigenvalue or Floquet analysis is carried out at each computed solution point, depending on the nature of the solution. For behaviour considered to be in equilibrium (fixed points), an eigenvalue analysis can be used, requiring local linearization in the case of a nonlinear system. Periodic behaviour (limit cycle oscillations - LCOs) on the other hand requires Floquet theory to determine stability (Ref. 28).

A bifurcation is a qualitative change in the system behaviour as a parameter is varied. In other words, when the stability of a system is changed or lost, the system bifurcates. The points at which these stability changes happen are called bifurcation points. If the system is nonlinear, new solution branches may emerge from the bifurcation points, leading to the presence of multiple solutions for a given set of system parameters. The identification of these different solution branches helps to uncover the global dynamics of the system. Of particular interest are instances where stability is dependent on the magnitude of a perturbation. The results of continuation analysis are displayed on bifurcation diagrams, where the values of solution branches are shown as the continuation parameter value varies. The type (equilibrium/periodic) of each solution branch, along with the location of any bifurcations it encounters, are also indicated. The solutions exist in a space whose number of dimensions is the number of states plus the number of continuation parameters. As this number is almost never less than the number of spatial dimensions, the convention is to make a 2D graph with the continuation parameter on the *x*-axis and the chosen state on the *y*-axis. The plotting of the solutions in terms of the chosen

quantities is known as a "projection" or a "plane". Where a state is used for the x-axis instead of the continuation parameter, the resulting plot is not considered a bifurcation diagram but rather a phase plane. Alternatively, if a 2-parameter continuation is made, the results can be plotted on a bifurcation diagram where both axes are parameters.

These analysis methods were employed according to the version of the system (linear/nonlinear) in question. Bifurcation diagrams were produced using the Dynamical Systems Toolbox for MATLAB by Coetzee (Ref. 29), which uses an implementation of AUTO-07P (Ref. 30). Time simulations were also used to corroborate the predictions of both stability methods. Differing sizes of the datum parameter values mean that it is most convenient to deal with quantities normalised against their datum values. Therefore, for the remainder of the present work all stiffness parameter values discussed refer to their normalised values without a change in notation.

RESULTS AND DISCUSSION

Linear Stability

Using eigenvalue analysis as described in the previous section allows the stability of a linear system to be quantified directly. Furthermore, the cause of any instability encountered can be identified through inspection of the location of the Jacobian's eigenvalues on the complex plane.

The concept of a stability boundary diagram between two parameters can be useful for understanding a sensitivity of a system's stability to changes in various parameters, particularly those that are readily controllable in the design phase of a practical system, such as a tiltrotor aircraft. Such a diagram can be produced from a grid of the combinations of different values for each parameter. The Jacobian matrix and its eigenvalues are calculated at each point, and a surface is overlaid on the grid whose height at each point is determined by the maximum real component of the Jacobian's eigenvalues there. As the sign of an eigenvalue determines the stability of the corresponding mode – positive being unstable – and only one unstable eigenvalue is required for overall system instability, a horizontal plane cut of this surface at the level 0 will produce a contour that denotes the boundary between the stable and unstable regions of the grid.

As aeroelasticity is such an important consideration during the design of tiltrotor aircraft, stability boundaries between structural parameters that are controllable to some degree are a useful tool for the designer. It is prudent to establish the stability boundary for the original linear system prior to any nonlinear modification to allow the identification of any changes caused by the presence of nonlinearities. To provide a simple basis for the introduction of the continuation methods employed in subsequent sections, a stability boundary between (linear) gimbal flapping stiffness K_β ($=\nu_\beta^2 I_b$) and wing torsional stiffness K_p is shown in Figure 6. In the equations of motion, the blade flapping stiffness is modelled implicitly using a normalised flapping natural frequency ν_β (i.e. per-rev). The axis is therefore labelled "effective" stiffness to reflect this adjustment.

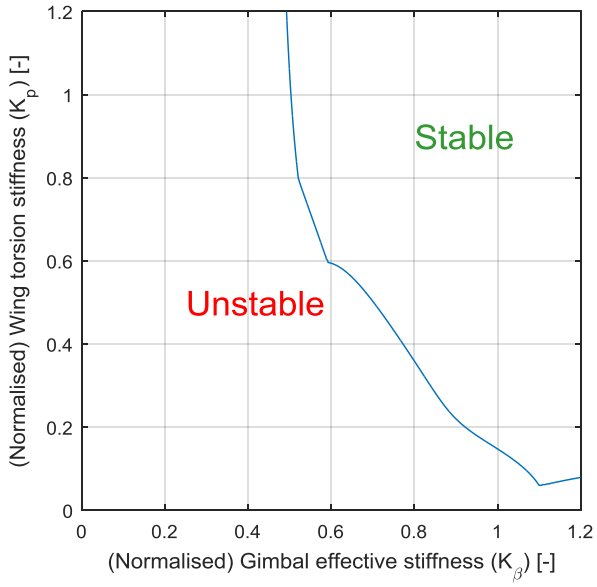

Figure 6: Stability boundary for the linear system between gimbal flapping stiffness and wing torsional stiffness.

The unstable region, that is, pairs of (K_β,K_p) values that will destabilise the system, is in the left portion of the figure. While Figure 6 does not reveal much information beyond the shape of the boundary, the sharpness of the corners at approximately K_β,K_p=(0.5, 1) and (1.1, 0.1) hints at the presence of three structures defining the boundary.

Bifurcation Analysis

Figure 6 can also be generated by continuation methods, as the system has an equilibrium at $\mathbf{X} = \mathbf{0}$ that can be used as a starting solution. Generating the stability boundary this way in fact affords deeper insight than the contour cut method. Key bifurcation types that are relevant to understanding the behaviour of a rotor-nacelle system, particularly when the nonlinear stiffness profiles are introduced, are *Hopf bifurcations* and *branch points* (Ref. 31). At a Hopf bifurcation, the stability of a fixed point (i.e. an equilibrium) changes, and a periodic solution arises, caused by a pair of complex conjugate eigenvalues crossing the complex plane imaginary axis. At a branch point, the solution changes stability, caused by a single real eigenvalue crossing over the complex plane imaginary axis. Because the branch points in this system are of the pitchfork type, two equilibrium branches emanate from the bifurcation point. For more information on the subject, the reader is referred to Ref. 31.

Choosing K_p=0.2 so that a continuation in K_β will intersect the regions of interest in the contour-based stability boundary in Figure 6, the bifurcation diagrams shown in

Figure 7 are obtained. In these diagrams, fixed point (equilibrium) solutions are plotted, with solid green denoting stability and dashed magenta denoting instability.

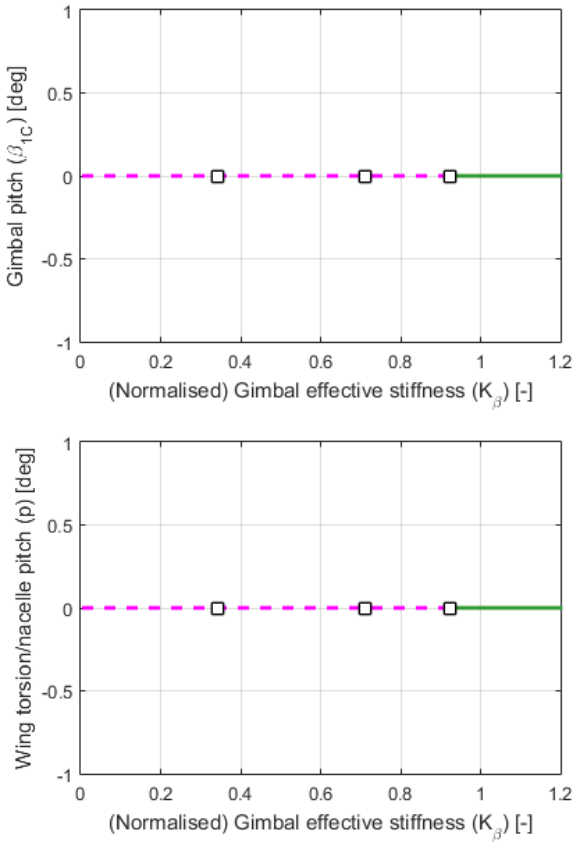

Figure 7: Bifurcation diagram (fixed points only) for K_p=0.2, for gimbal pitch β_{1C} (top) and wing torsion p (bottom) with K_β as the continuation parameter.

Note the three Hopf bifurcations at K_β =0.34, 0.71 and 0.92 (square icons). These points correspond to the intersections of a line at K_p=0.2 with the unstable region of Figure 6, indicating that the boundary of the unstable region is defined by the loci of the various bifurcations. The bifurcations are visible at the same points in the projections of β_{1C} and p. These states were chosen to give as complete as possible a picture of the dynamics of the whole wing-nacelle system. Both states remain zero throughout the continuation as it corresponds to system in its undeformed state.

As the system is unstable from the right-most Hopf moving leftward, the additional Hopf bifurcations denote changes in the stability of further modes of the system beyond that associated with the right-most one. Figure 8 shows the wing torsion projection from Figure 7 with the damping ratios of the system's modes over the same sweep of K_β.

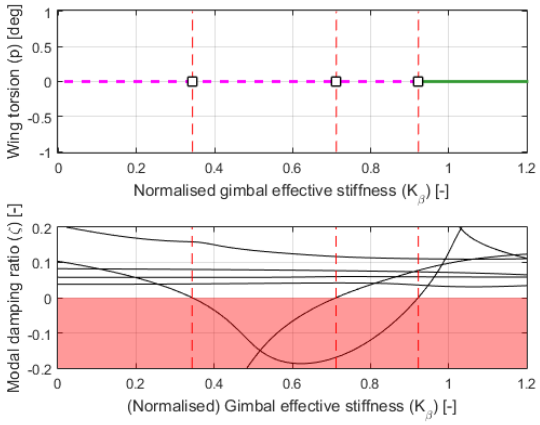

Figure 8: Bifurcation diagram (equilibria only, top) for K_p=0.2, for wing torsion p, with K_β as the continuation parameter, with the damping ratio of the system's eigenvalues over the same range of K_β (bottom).

In order to fully reconstruct Figure 6 through continuation, bifurcation diagrams of the equilibria, like Figure 7, can be generated for several different values of K_p. Alternatively, a two-parameter continuation in K_p and K_β can be performed on the Hopf bifurcations to trace their loci in the K_p-K_β plane, and this method is employed here. Plotting these continuations, shown in Figure 9, reconstructs the stability boundary obtained in Figure 6. Now however, the significance of each part of the boundary is known, as well as the path of each segment once inside the unstable region.

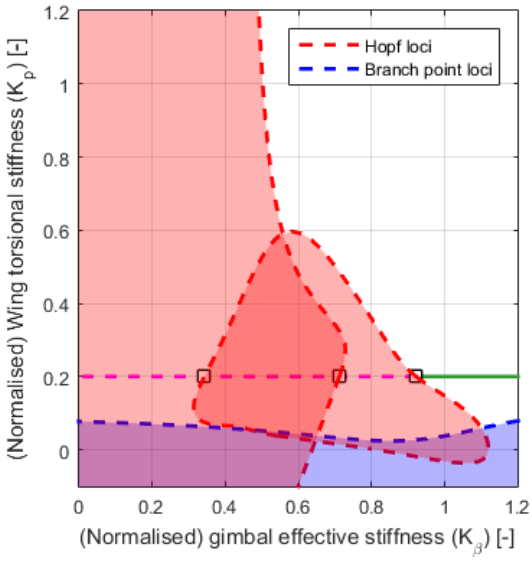

Figure 9: Stability boundary between wing torsional stiffness K_p and gimbal effective stiffness K_β, generated by two-parameter continuation. All shaded areas are unstable.

While the following of one of the Hopf bifurcations into negative wing stiffness K_p values may seem unusual, it is typical in bifurcation analysis to extend the continuation outside the physical range to search for the connection of any branches that would otherwise not be visible.

Both Figure 8 and Figure 9 show that several of the Hopf bifurcations observed in Figure 7 are connected. Focusing on Figure 9, the right-most and left-most Hopfs are connected via a loop that forms the middle portion of the boundary (between stable and unstable regions). Meanwhile, the middle Hopf does not share its loci with any other bifurcations, at least within the area of analysis. All points that lie within this region have periodic solutions in β_{1C} and p (and in fact all the state variables) – and these motions are the whirl flutter that this paper concerns.

The following sections use continuations in K_β, at K_p values of 1.1 and 0.2, in the wing torsion (p) state and gimbal pitch (β_{1c}) projections. The higher value could correspond to an alternate tiltrotor design with increased wing torsional stiffness compared to the baseline version, and the lower value might represent a damage case.

Defining Whirl Flutter

Typically, whirl flutter is introduced using the basic model set forth by Reed in Ref. 22.

A 2-DoF system, a rotor disc spins about the end of a shaft which may move in pitch and yaw about an effective pivot point, with associated stiffness and damping properties in each of these degrees of freedom. The rotor is not able to move relative to the shaft in any other way, and the aerodynamics are quasi-steady, derived from strip theory. With equation terms relevant to the various physical phenomena that drive the whirl flutter instability, the model captures whirl flutter dynamics succinctly. The two modes of the system are both whirl flutter modes: forward whirl (where the whirl is in the same direction as the rotor spin) and backward whirl (vice versa). Increasing pivot stiffness and damping stabilises the system, while increasing inertias and airspeed destabilises the system. The aerodynamics model features spring coupling between shaft pitch and yaw, and destabilisation of the system through increasing gyroscopic influence is only possible if this spring coupling is retained. In this model, only the backward whirl mode may become unstable.

As almost all nine modes of the system are oscillatory (the one exception being the mode Johnson names 'ζ'), it may be tempting to consider any periodic solution to be whirl flutter. However, the dynamics of a gimballed prop-rotor (i.e. one with flapping blades) bear little resemblance to those of Reed's canonical whirl flutter demonstration model. For instance, the ability of the blades to flap permits a higher whirl flutter onset speed, though the forward whirl mode may also experience instability.

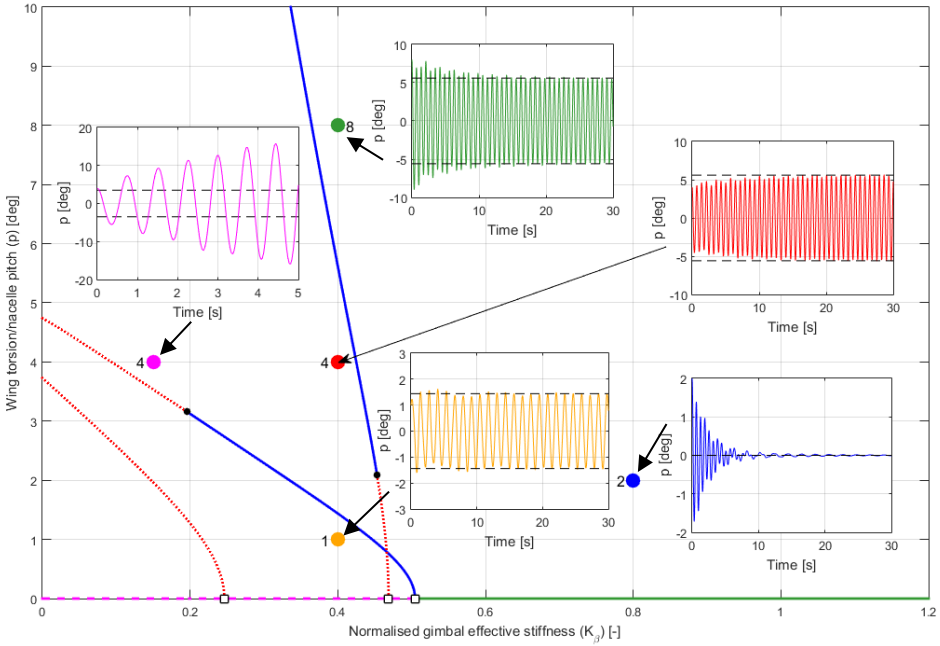

Figure 10: Bifurcation diagram for hardening blade flapping, case 1 (K_p=1.1), with K_β as the continuation parameter, with time simulations started at a selection of K_β values. Initial conditions are shown with coloured dots

Modern literature investigating whirl flutter in gimballed rotor-nacelle systems, such as Refs. 1, 8 and 9, tends to present stability arguments in terms of wing modes. As it is typically the wing structure that experiences failure in the event of whirl flutter occurring, this definition seems logical and so has been adopted in the present work. A full analysis

of the Johnson model's modes in order to categorise them as whirl flutter is beyond the scope of the present research. Furthermore, such a categorisation is inappropriate as the periodic solutions found through continuation analysis will be unspecified varying mixtures of the system's modes. Additionally, only three of the system's modes (q_1, q_2, p) are found to experience instability within the range of the present work, and all are found to contain prevalent wing motion.

Effects of Cubic Hardening (K_2=10, K_3=0)

Examining cubic hardening first, case 1 (K_p=1.1) is initially considered and a full bifurcation diagram including periodic solution branches is presented in Figure 10. The figure shows complex behaviour manifested in stable and unstable limit cycles and secondary equilibrium branches. As the Hopf and branch point are both on the equilibrium branch which lies at zero displacement, the positions of the bifurcations do not change with the addition of any nonlinear stiffness terms. However, the dynamic behaviour outside the equilibrium branch calculated in Figure 7 (hereafter referred to as the 'main branch') is affected by nonlinear terms.

While bifurcation analysis is able to illuminate complex and/or hidden behaviour of a system, the best approach is to supplement continuation with time simulations at points of interest for a fuller understanding. Bifurcation analysis is able to uncover unstable branches that might be difficult or practically impossible to find through time simulations, while time simulations give a sense of how strongly attractive or repulsive a point on a stable or unstable solution branch is, respectively – something indirectly quantified by bifurcation analysis but not typically displaced on bifurcation diagrams. Time histories are shown in Figure 10 for a number of values of K_p, with different initial conditions to demonstrate the stability of limit cycles by showing convergence or divergence as relevant. From right to left, the areas of interest that are selected for time simulation are the undeformed equilibrium branch (demonstrating convergence from a small perturbation), stable flutter having emanated from the Hopf bifurcation at approximately K_β=0.46 (demonstrating convergence on a limit cycle with an amplitude of 5.5°), lower-amplitude stable flutter having emanated from the Hopf bifurcation at approximately K_β=0.5, and unstable growing periodic motion from the near vicinity of an unstable periodic solution branch at K_β=0.15. For periodic solutions, solid blue denotes the peak amplitude of stable limit cycles, and dashed red denotes the peak amplitude of unstable limit cycles. Only the projection in wing torsion p is shown here, though projections in any of the other state variables could also be plotted. Limit points are denoted by a black dot and reflect a change in stability of a solution branch which folds back at the bifurcation point, changing direction in the solution space. A full key to the bifurcation diagrams is shown in .

Table 2: Key to bifurcation diagrams

Graphic	Description	Meaning
	Solid green line	Stable equilibrium branch
	Dashed magenta line	Unstable equilibrium branch
	Solid blue line	Stable periodic solution (max. value)
	Dashed red line	Unstable periodic solution (max. value)
□	Hollow square	Hopf bifurcation
●	Black circle	Limit point (fold) bifurcation
★	Black star	Branch point bifurcation

For some portions of the main branch where it has become unstable (e.g. K_β=*0.4*), the nonlinearity has created two stable periodic solutions which the system may be attracted to, depending on initial conditions.

Establishing a way of describing the theoretical findings of bifurcation analysis in terms of the practically oriented language of aeroelasticity requires special care, despite the purportedly qualitative nature of both fields. The principal issue is the stability of solutions. When observed in practice, static divergence and whirl flutter are almost always immediate, irreversible "runaway" unstable motions. However, in continuation analysis, both stable and unstable solution branches may be found for both equilibrium and periodic solutions. The unstable solution branches are precise "knife-edge" cases and may be difficult or impossible to find through time simulations. This leads to apparently contradictory terminology being used to describe the various types of behaviour observed in the model; the phrase "stable static divergence" is a contradiction in terms when viewed from the standpoint of aeroelasticity, though in the domain of bifurcation theory it refers quite clearly to a whirl flutter periodic solution branch that can attract the system state within some neighbourhood around it. In order to preserve both the physical meaning of predicted behaviour and the insights afforded by bifurcation analysis, the terms "static divergence" and "whirl flutter" are used in direct conjunction with terms qualifying stability throughout the discussion sections of this work.

Full bifurcation diagrams for both K_p cases generated using a hardening blade flapping stiffness profile (K_2=10, K_3=0) and are shown in Figure 11. Each of the diagrams can be cross-referenced with Figure 9 to confirm that the bifurcations present correspond to the extent of the unstable regions at the relevant value of K_β. As the value of blade flapping stiffness is gradually decreased, the amplitude of the limit cycles increases to quite an extent.

While the fold bifurcations seen don't involve a change of direction of the solution branch within the plane, there will be such a direction change in one of the other states'

projection. In Figure 11a, β_{1c} projection, the fold bifurcation on the limit cycle branch emanating from the Hopf bifurcation near K_β=0.45 is unrelated to the nearby crossing of this branch with the limit cycle branch emanating from the right-most Hopf, as is evident from the p projection where the branches are more clearly separate.

The hardening stiffness profile has the general effect of bending all the periodic solution branches leftward. The branches emanating from the various Hopf bifurcations observed in each of the bifurcation diagrams shown can be expected to connect in the same manner described by Figure 9.

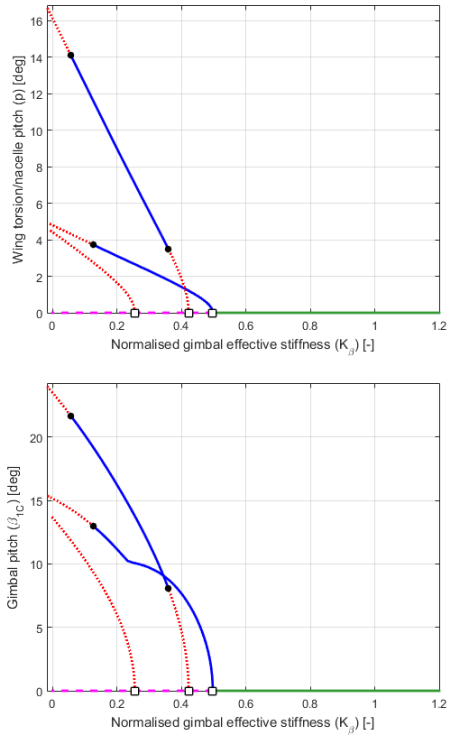

Figure 11a: Bifurcation diagram for case 1 (K_p=1.1), hardening system (K_2=10, K_3=0)

While Figure 11a shows three LCO branches bent leftward by the hardening nonlinearity, Figure 11b indicates considerably richer dynamics. The LCO branch emanating from the right-most Hopf bifurcation folds over itself a number of times, experiencing a variety of fluctuations in the maximum amplitudes of its various states before bending leftward as a stable branch.

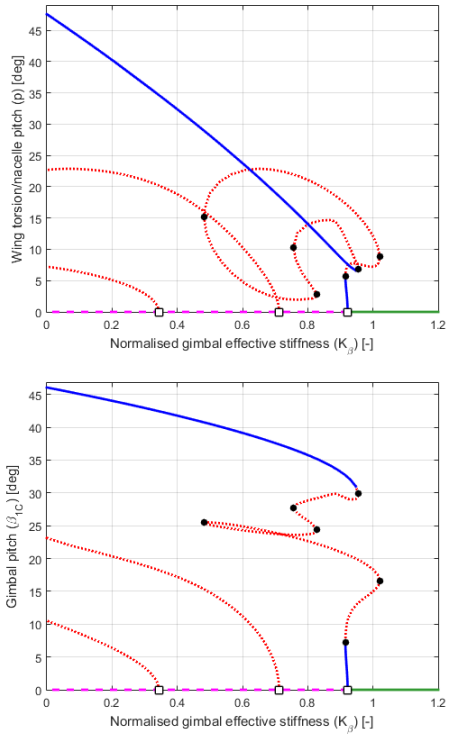

Figure 11b: Bifurcation diagram for case 2 (K_p=0.2), hardening system (K_2=10, K_3=0)

Effects of Varying K_2

In the above cases, a value of cubic nondimensional stiffness coefficient K_2 was selected rather arbitrarily in order to effect nonlinear stiffness behaviour. It would therefore be prudent to understand the effect of the size of K_2's value. Bifurcation diagrams with K_p set to 1.1 (as per case 1) for increased and decreased values of K_2 are shown in Figure 12 and Figure 13. As is evident from the plots, increasing K_2 decreases the amplitude of the flutter and for a given value of K_β, due to increasing K_2 making the structure stiffer.

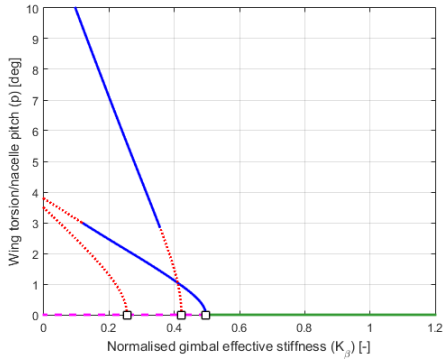

Figure 12: Bifurcation diagram for case 1 (K_p=1.1), K_2=16, K_β as continuation parameter.

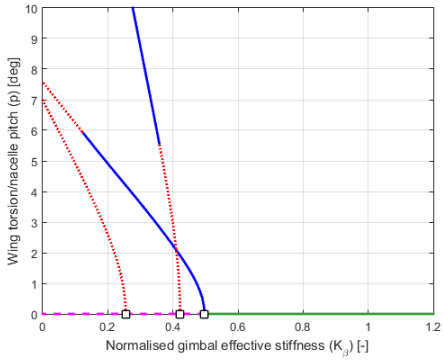

Figure 13: Bifurcation diagram for case 1 (K_p=1.1), K_2=4, K_β as continuation parameter.

The effects of changing K_2 could also be explored for the other cases of K_p, though this is deemed outside the scope of this paper.

Effects of Cubic Softening (K_2= -10, K_3=0)

To examine the effect of softening in the blade flapping stiffness, bifurcation diagrams with K_2=-10, K_3=0 are shown in Figure 14.

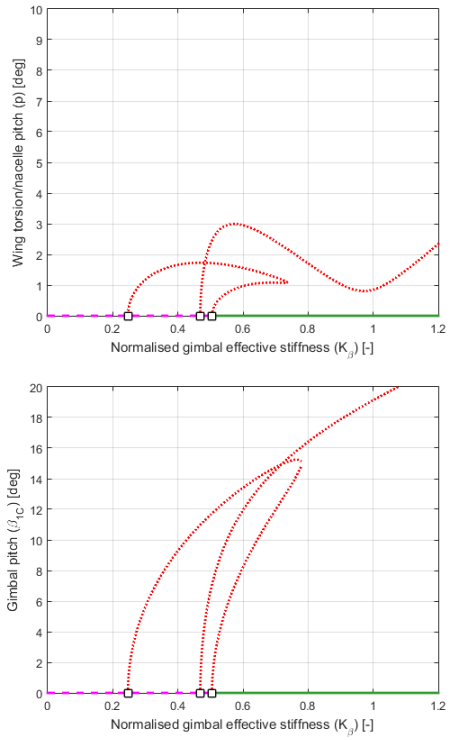

Figure 14a: Bifurcation diagram for case 1 (K_p=1.1), softening system (K_2= -10, K_3=0)

The overhanging of the main branch with an unstable periodic solution branch in Figure 14a presents a divergence hazard as it is not clear from the plot where the system will be attracted to if it is perturbed in this direction. Figure 14b shows rich dynamics manifested in multiple periodic solution branches that overlap generously in several of the projections. While not relevant to the focus of the present work, it is worth noting the branch points on the larger periodic solution branches. These link two further periodic solution branches to that which connects to the Hopf bifurcations on the main branch. Interestingly, no stable overhang of the main branch is observed in either of the two K_p cases, despite softening stiffness profiles causing overhang in Ref. 19. As expected, the joining between Hopfs is in accordance with Figure 9, as the paired Hopfs correspond to the same specific modal instability.

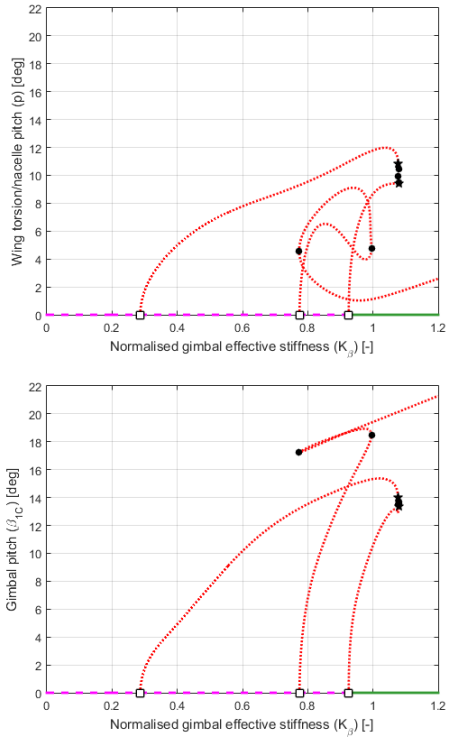

Figure 14b: Bifurcation diagram for case 2 (K_p=0.2), softening system (K_2= -10, K_3=0)

Effects of Combined Cubic Softening – Quintic Hardening (K_2= -10, K_3=100)

Introducing a positive quintic coefficient (K_3) into the softening stiffness profile used in the previous section allows softening effects to dominate at lower deflections and hardening effects at higher deflections. Compared with the softening model's results, the hardening effects bend the static divergence branches back round to the left, allowing a small branch of flutter LCO's to exist on each, as seen in the hardening model. Using a K_3 value of 100, the bifurcation

diagram results for the combined softening-hardening profile implemented in the blade flapping stiffness are shown in Figure 15.

The effect of K_3 is similar to the effect of K_2 in that a larger value makes for a stiffer structure than a lower value, and the effect is to restrict the amplitude of periodic solutions. As in the Cubic Softening sub-section, a more detailed investigation into the influence of K_3 could be carried out, varying other parameters such as K_p and K_2, though this is deemed beyond the scope of the study presented in this article.

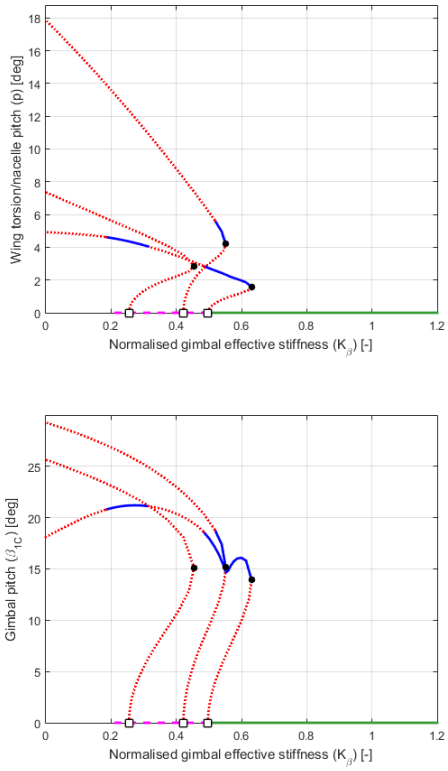

Figure 15a: Bifurcation diagram for case 1 (K_p=1.1), combined system (K_2= -10, K_3=100)

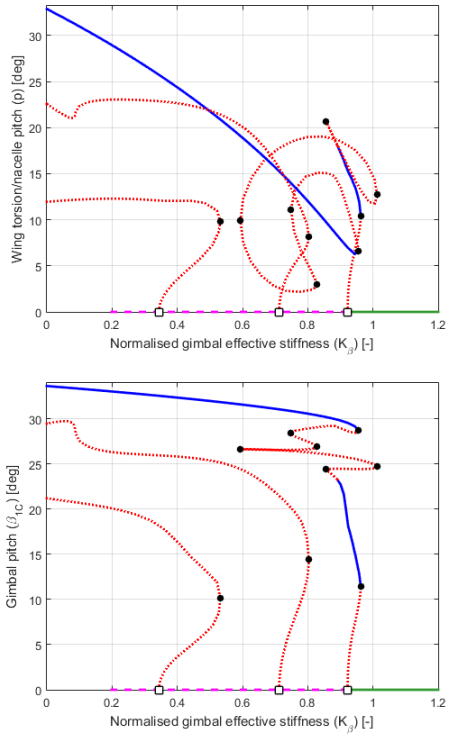

Figure 15b: Bifurcation diagram for case 2 (K_p=0.2), combined system (K_2= -10, K_3=100)

Both cases contain overhang within the range of analysis, originating from both the centre and right-most Hopf bifurcations. As these Hopf bifurcations correspond to different modal instabilities, it may be expected that limit cycles taken from each of these stable portions would be qualitatively different to each other. This is corroborated by the figure at least as far as amplitude is concerned: the amplitude of the first instance of whirl flutter (when decreasing K_β) met is of notably smaller amplitude than that of the second instance. A rotor nacelle mounted on an aircraft is subject to perturbations, either from manoeuvring or gusts. A perturbation of the rotor-nacelle may ultimately bring it sufficiently close to either of these solution branches to experience behaviour of either type. The linear stability analysis has therefore failed to predict the above result. The flutter boundary predicted by this method is the location of the Hopf bifurcation near K_β=0.5, though whirl flutter behaviour is shown to exist for values of K_β that lie within the stable region.

Impact on Stability Boundary

In all cases for all nonlinear models, the linear analysis correctly finds the point on the main branch at which whirl flutter branches emerge. However, as shown in the combined model, there are stable portions of whirl flutter branches overhanging the main branch in parameter ranges that the linear analysis predicted to be stable. In practical terms, this means that the system is able to experience whirl flutter in these supposedly stable parameter value ranges. Figure 16

shows the link between overhang and the stability boundary. The top part of the figure is an excerpt from the bifurcation diagram for the combined model, case 1 (K_p=1.1), showing the overhang of a stable region of the whirl flutter branch over the main branch. The corresponding extent of this overhang in K_θ is shown on the stability boundary in the bottom part of the figure.

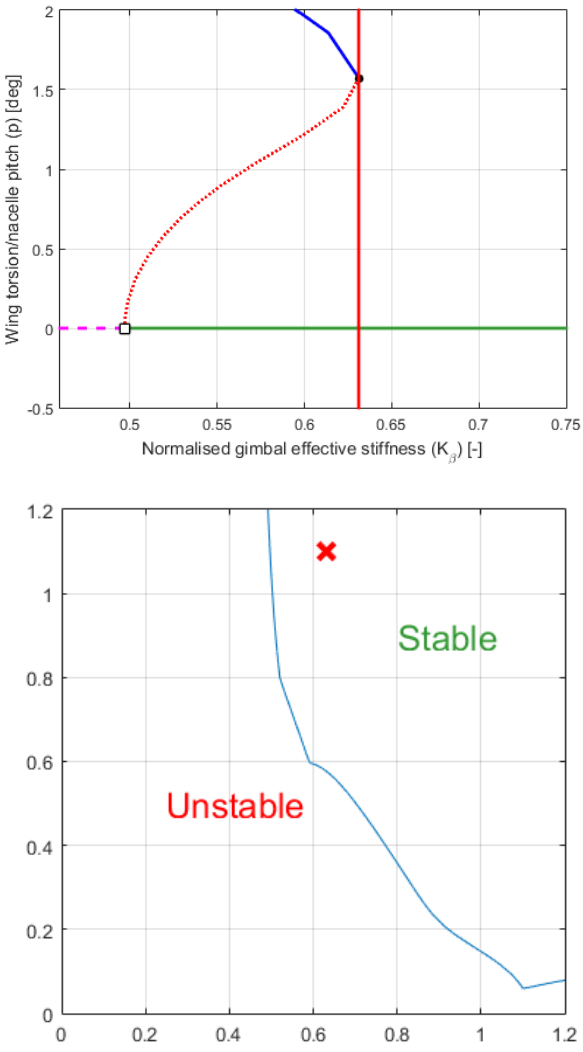

Figure 16: Stable portion of whirl flutter branch overhanging stable main branch for combined system, with corresponding location on the K_p-K_θ stability boundary

The extent of the stable (i.e. attracting) whirl flutter branch into the stable main branch regions means that the system cannot be said to be stable in the affected parameter value range. As the system is only truly safe from whirl flutter above the right-most extent of the overhanging stable branch, it is logical to redraw the stability boundary to take account of this overhanging effect. This could be achieved either through running several continuations in K_β at various values of K_p to record the overhang extent at each level, or through two-parameter continuation of the limit point bifurcation on the whirl flutter branch that defines this extent. The redrawn stability boundary is shown in Figure 17.

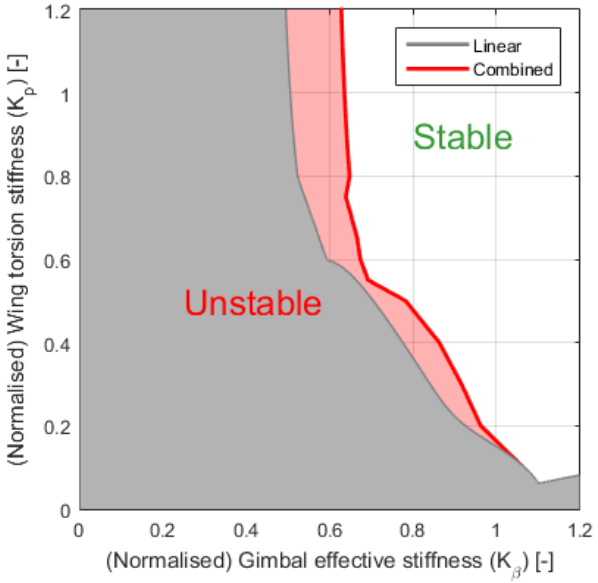

Figure 17: Redrawn K_p-K_β stability boundary to take account of overhang caused by combined nonlinearity in blade flapping stiffness, compared to the baseline linear stiffness boundary. The additional unstable area is shaded in red.

The discontinuity in the boundary near K_p=1 is due to the point change in the number and type of Hopf bifurcations present in a continuation in K_β, which affects the origin of the overhanging branches. Above K_p=1, there are three Hopf bifurcations corresponding right to left to the q_2, p and q_2 (again) mode instabilities. Below K_p=1 however, there are five, corresponding to the q_1 mode instabilities. The qualitative point change in the structure of these instabilities causes a corresponding point change in the origin and extent of any overhang present. The overhang disappears at approximately K_p=0.15.

While the paper has made a point of stable overhanging whirl flutter branches posing a hazard to stability, unstable branches can also pose a threat. Continuation and bifurcation methods do not map out regions of attraction or repulsion in the region of solution branches, let alone within the solution manifold as a whole, so time simulations would be needed to investigate the behavioural impact of the presence of the overhanging unstable whirl flutter branches in the softening system, in both cases of K_p (Figure 11).

CONCLUSIONS

1. This paper has demonstrated the use of a basic gimballed rotor-nacelle system model for dynamic analysis of whirl flutter behaviour. Both linear and nonlinear stiffness profiles were used for the gimbal flapping stiffness through addition of cubic and quintic terms.
2. Stability analysis methods were described and employed for linear and nonlinear models.
3. Bifurcation diagrams were generated for the hardening, softening and combined cases of both stiffness nonlinearities, and cases were shown where whirl flutter was possible in a region where linear analysis predicts local stability. In some cases, a perturbation of just one or two degrees is enough to take the system outside of the local basin of attraction.
4. The stability boundaries were redrawn to take account of this phenomenon, which appended an extra region of instability to the existing unstable region.
5. The portions of the overhanging whirl flutter branches found to be stable by continuation analysis only refers to the fact that attracting LCOs exist, and allowing a real world tiltrotor system to encounter them should not be thought of as viable.
6. Where whirl flutter does not cause the loss of an aircraft, oscillations induced by whirl flutter present a fatigue hazard to aircraft structures, such as the nacelle mounts.
7. Overhanging of unstable whirl flutter branches arguably presents a greater hazard as without a full bifurcation diagram for the system it is not clear where it will be attracted to if a perturbation is experienced in the vicinity of the overhanging branch.
8. These findings therefore emphasise the importance of using proper nonlinear analysis methods in conjunction with models that fully capture important nonlinear effects in a system of interest.
9. Regarding future work, a natural progression from the present work would be a similar analysis of the effects of structural nonlinearity at the wing, both as a stiffness nonlinearity originating from the wing structure and as a freeplay nonlinearity originating from the tilting mechanism.

Author contact: Christopher Mair chris.mair@bristol.ac.uk
Djamel Rezgui djamel.rezgui@bristol.ac.uk
Branislav Titurus brano.titurus@bristol.ac.uk

ACKNOWLEDGMENTS

The authors would like to kindly thank The UK Engineering and Physical Sciences Research Council (EPSRC) for funding this research project.

REFERENCES

1. Acree C. W., and Johnson W., "Aeroelastic Stability of the LCTR2 Civil Tiltrotor", AHS Technical Specialists' Meeting, Dallas, TX, October 15-17, 2008.
2. https://en.wikipedia.org/wiki/Bell_XV-15#/media/File:Bell-NASA_XV-15_(cropped).jpg. Accessed August 2018.
3. Various authors, "Braniff Airways Flight 542 Aircraft Accident Report", Civil Aeronautics Board Report SA-346, 1961.
4. Kunz D. L., "Analysis of Proprotor Whirl Flutter: Review and Update", *Journal of Aircraft*, Vol. 42, (1), 2005, pp. 172-178. DOI: 10.2514/1.4953.
5. Richardson D. A., "The Application of Hingeless Rotors to Tilting Prop/Rotor Aircraft", *Journal of the American Helicopter Society*, Vol. 16, (3), 1971, pp. 34-38.
6. Bielawa R. L., *Rotary Wing Structural Dynamics and Aeroelasticity*, Second Edition, AIAA Education Series, Washington, DC, 2005, pp. 387-433.
7. Nitzsche F., "Whirl-Flutter Suppression in Advanced Turboprops and Propfans by Active Control Techniques", *Journal of Aircraft*, Vol. 31, (3), 1994, pp. 713-719.
8. Acree C. W., Peyran R. J., and Johnson W., "Rotor Design Options for Improving Tiltrotor Whirl-Flutter Stability Margins", *Journal of the American Helicopter Society*, Vol. 46, (2), 2001, pp. 87-95. DOI: 10.4050/JAHS.46.87.
9. Acree C. W., "Effects of V-22 Blade Modifications on Whirl Flutter and Loads", *Journal of the American Helicopter Society*, Vol. 50, (3), 2005, pp. 269-278.
10. Park J. S., Sung N. J., Myeong-Kyu L., and Kim J. M., "Design Optimization Framework for Tiltrotor Composite Wings Considering Whirl Flutter Stability", *Composites Part B: Engineering*, Vol. 41, (4), 2010, pp. 257-267. DOI: 10.1016/J.COMPOSITESB.2010.03.005.
11. Janetzke D. C., and Kaza K. R. V., "Whirl Flutter Analysis of a Horizontal-axis Wind Turbine with a Two-bladed Teetering Rotor", *Solar Energy*, Vol. 31, (2), 1983, pp. 173-182. DOI: 10.1016/0038-092x(83)90079-8.
12. Masarati P., Piatak D. J., and Quaranta G., "Soft-inplane Tiltrotor Aeromechanics Investigation Using Two Comprehensive Multibody Solvers", *Journal of the American Helicopter Society*, Vol. 53, (2), 2008, pp. 179-192.
13. Krueger W. R., "Multibody Analysis of Whirl Flutter Stability on a Tiltrotor Wind Tunnel Model", *Proc. of the Institution of Mechanical Engineers, Part K: Journal of Multi-body Dynamics*, Vol. 230, (2), 2014, pp. 121-133.
14. Lee B.H.K., and Tron A., "Effects of Structural

Nonlinearities on Flutter Characteristics of the CF-18 Aircraft", *Journal of Aircraft*, 1989. DOI: 10.2514/3.45839.

15. Jutte C.V., and Kota S., "Design of Nonlinear Springs For Prescribed Load-Displacement Functions". *J. Mech. Des*., 2008. DOI: 10.1115/1.2936928.
16. Rezgui D., and Lowenberg M. H., "On the Nonlinear Dynamics of a Rotor in Autorotation: a Combined Experimental and Numerical Approach", *Phil. Trans. R. Soc. A*, 373.2051 20140411, 2015. DOI: 10.1098/RSTA.2014.0411.
17. Rezgui D., Lowenberg M. H., Jones M., and Monteggia C., "Continuation and Bifurcation Analysis in Helicopter Aeroelastic Stability Problems", *J. Guid. Control Dyn.*, Vol. 37, 2014, pp. 889–897.
18. Jones M., Bernascone A., Masarati P., Quaranta G., and Rezgui D., "Ongoing Developments in the Use of Continuation-Bifurcation Methodology at AgustaWestland" , Proc. 40th European Rotorcraft Forum, 2014, pp. 905-918.
19. Mair C., Rezgui D., and Titurus B., "Nonlinear Stability Analysis of Whirl Flutter in a Tiltrotor Rotor-Nacelle System", Proc. 34th European Rotorcraft Forum, Milan, 2017.
20. Mair C., Rezgui D., and Titurus, B., "Nonlinear Stability Analysis of Whirl Flutter in a Rotor-Nacelle System", *J. Nonl. Dyn.*, Vol. 94, (3), 2018, pp. 2013-2032. DOI: 10.1007/s11071-018-4472-y.
21. Carlson R., and Miao W., "Aeroelastic analysis of the elastic gimbal rotor", NASA Contract Report 166287, 1981.
22. Reed W. H. III, "Propeller-Rotor Whirl Flutter: A State-of-the-Art Review", Symposium on the Noise and Loading Actions on Helicopters, V/STOL, and Ground Effect Machines, The University of Southampton, England, August 1966. DOI: 10.1016/0022-460x(66)90142-8.
23. Johnson W., "Dynamics of a tilting proprotor aircraft in cruise flight", NASA Technical Note D-7677, 1974.
24. Johnson W., "Analytical modeling requirements for tilting proprotor aircraft dynamics", NASA Technical Note D-8013,1975.
25. Johnson W., "CAMRAD/JA: A comprehensive analytical model of rotorcraft aerodynamics and dynamics, Theory Manual", Johnson Aeronautics, 1988.
26. Ribner H.S., "Propellers in Yaw", NACA Report 820, 1945.
27. MATLAB 2015a, The MathWorks, Inc., Natick, Massachusetts, United States
28. Kuchment P. A., *Floquet Theory for Partial Differential Equations*, Vol. 60. Birkhäuser, Basel, 2012. DOI: 10.1007/978-3-0348-8573-7.
29. Coetzee, E., Krauskopf, B., and Lowenberg, M.: "The dynamical systems toolbox: Integrating AUTO into MATLAB", Proc. 16th US National Congress of Theoretical and Applied Mechanics USNCTAM2010-827, 2010.
30. Doedel E. J., Fairgrieve T. F., and Sandstede B., "AUTO-07P: Continuation and bifurcation software for ordinary differential equations", 2007.
31. Kuznetsov Y.A., *Elements of Applied Bifurcation Theory*, Third Edition, Springer Science & Business Media, New York, 2004. DOI: 10.1007/978-1-4757-3978-7.
32. du Bois J. L., Adhikari S., and Lieven N. A. J., "On the quantification of eigenvalue curve veering: a veering index", *J. Applied Mechanics*, Vol 78, (4), 041007, 2011. DOI: 10.1115/1.4003189.